Science Advances

Supplementary Materials for

Single-molecule photocatalytic dynamics at individual defects in two-dimensional layered materials

Teng-Xiang Huang, Bin Dong, Seth L. Filbrun, Aisha Ahmad Okmi, Xiaodong Cheng, Meek Yang, Nourhan Mansour, Sidong Lei*, Ning Fang*

*Corresponding author. Email: nfang@xmu.edu.cn (N.F.); slei@gsu.edu (S.L.)

This PDF file includes:

Sections S1 to S10
Figs. S1 to S19
Table S1
References

Section S1. Experimental setup for single-molecule study on 2D layered InSe.

Single-molecule fluorescence imaging experiments were carried out on a prism-type total internal reflection fluorescence (TIRF) microscope (Fig. S1). A 365 nm UV light (127 mW cm^{-2}) vertically illuminates onto the sample to excite the photogeneration of electrons and holes. An adjustable 60 mW, 488 nm CW laser (Oxxius, Lannion, France) with p-polarization was focused on the interface between the aqueous solution and the quartz slide by a focusing lens, generating a focal spot size of 60 μm × 100 μm. The fluorescence signal was collected by a high numerical aperture water-immersion objective (60×, NA = 1.2, Olympus) and focused onto an Andor iXonEM+ Ultra 897 camera (Belfast, Northern Ireland: 512 × 512 imaging array, 16 μm × 16 μm pixel size). A fluorescence filter set composed of a laser quad band set (Chroma 89901-ET-405/488/561/640 nm) and a 535/50 nm bandpass filter (Semrock) was used to reject the scattering signal from the background.
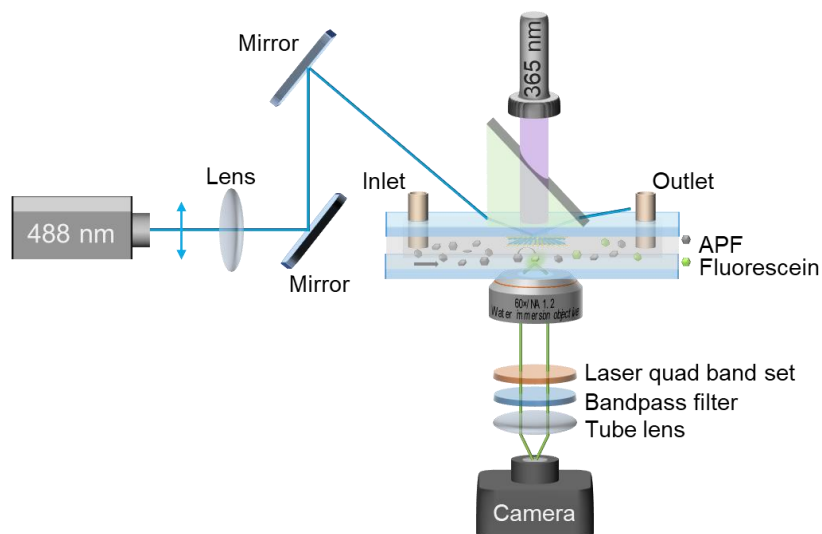

Fig. S1. Prism-type total internal reflection microscope with a flow chamber setup.

Mechanically exfoliated 2D layered InSe flakes were transferred onto a quartz slide as catalysts. The sample slide and a #1.5 coverslip were then assembled to a flow chamber with dimensions of 40 mm × 4 mm × 0.12 mm (Fig. S1) using double-sided tapes. During the imaging experiments, a steady stream of the mixture (0.02~1 μM 3-Aminophenyl fluorescein (APF) in 10 mM pH 7.4

phosphate-buffered saline (PBS) buffer) was introduced into the flow chamber using a syringe pump for continuously supplying a constant concentration of reactants over 2D layered InSe. The flow rate was set to 20 μL min^{-1}. Highly fluorescent fluorescein product molecules were formed on 2D layered InSe and recorded with an exposure time of 100 ms.

Section S2. Ensemble measurements of photocatalytic activity of 2D layered InSe.

To measure the photocatalytic activity of 2D layered InSe, a fluorogenic oxidation reaction of weakly fluorescent APF to produce highly fluorescent fluorescein (λ_{ex}: 488 nm, λ_{em}: 513 nm, at pH 7.4) (Fig. S2A) was used. Ensemble-averaged fluorescence emission spectra was performed by a spectrofluorometer (Perkin Elmer LS55) and employed to evaluate the photocatalytic activity of InSe flakes. First, bulk InSe crystal was synthesized by using a nonstoichiometric melt of In and Se(*53*). The bulk InSe (~2 mg) was then mechanically cleavage by ultrasonication in ethanol (2 mL) to produce InSe flakes suspension. 10 μL InSe flakes suspension was mixed with 3 mL mixture of 1.6 μM APF and 10 mM PBS buffer (pH 7.4). When the mixture was exposed to light (365 nm UV and 488 nm laser), a new fluorescence peak appeared at 513 nm (Fig. S2B) and its intensity increased remarkably with the increase of irradiation time (Fig. S2C). In control experiments, the increase in fluorescence intensity was negligible when either InSe or light was absent (Fig. S2C). The above study indicates the photocatalytic ability of InSe to convert APF to fluorescein.
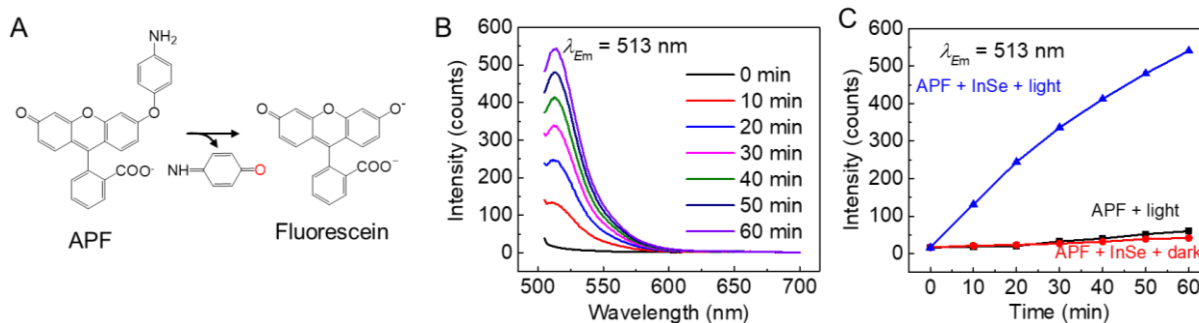
Fig. S2. Ensemble measurement of photocatalytic activity of InSe flakes. (A) APF is converted to fluorescein by reacting with hydroxyl radical. (B) Fluorescence spectra measured before and after light irradiation (365 nm light and 488 nm laser) of the PBS buffer containing APF and InSe. (C) Time-dependent fluorescence intensity of fluorescein with and without InSe and light. λ_{ex}: 488 nm, λ_{em}: 513 nm.

It has been demonstrated that ·OH can convert APF to fluorescein whereas other reactive oxygen species such as $O_2^{·-}$ and $HO_2^{·}$ cannot oxidize APF(*56*). However, after introducing the ·OH

scavenger (dimethyl sulfoxide, DMSO), APF can still converse to fluorescein, but the reaction rate significantly decreases (Fig. S3). This indicates that another reaction pathway exists. Takashi et al.(*18*) found that photogenerated hole can directly react with APF without the ·OH intermediate, which may exist another possible reaction pathway on InSe. Although the predominat reaction mechanism is still unclear and beyond the scope of this work, the nature of this photocatalytic reaction is the reaction between APF and photogenerated electron/hole. Therefore, we can still use APF to probe the photocatalytic activity of InSe.
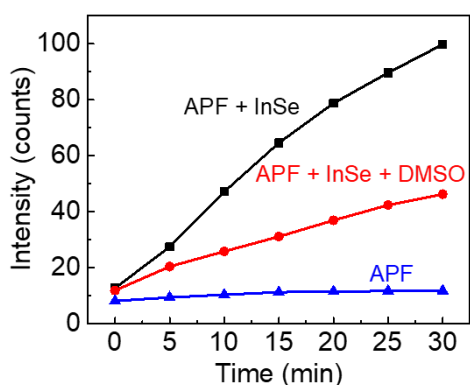

Fig. S3. Time-dependent fluorescence intensity of fluorescein with and without 2 mM DMSO. Photocatalysis was performed under the irradiation of 365 nm light. Fluorescence measurement: λ_{ex}: 488 nm, λ_{em}: 513 nm.

Section S3. Localize single-molecule catalytic events with nanometer precision.

Fig. S4 exhibits a segment of another fluorescence intensity trajectory, it clearly shows that the single molecule emitter only has one on-step (right), whereas multiple molecules show multiple on-steps (left). The multiple on-steps indicates a new fluorescein molecule is generated on the same site before the earlier one dissociates. These events have very low population in our imaging experiments and were excluded from quantitative analysis of reaction kinetics.
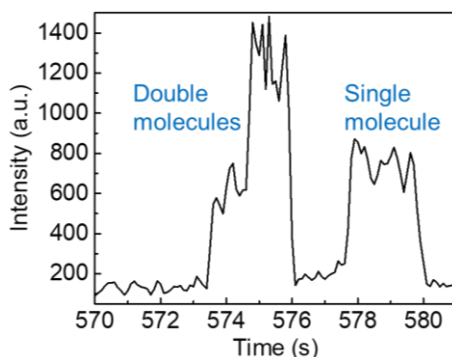
Fig. S4. A segment of fluorescence intensity trajectory shows that multiple catalytic reactions could happen within the same on-off cycle.

Fig. S5A is a typical fluorescence image of a single fluorescein molecule on InSe in our imaging experiments. The fluorescence intensity spreads over a few pixels as a point spread function (PSF) and the positions of identified molecule in every imaging frame were localized by using a similar approach published previously(*15*). Briefly, the single-molecule image can be fitted with 2D elliptical Gaussian functions for determining its center position (Fig. S5B):

$$I(x, y) = A + B * exp\left(-\left(\frac{(x-x_0)^2}{2S_x^2} + \frac{(y-y_0)^2}{2S_y^2}\right)\right)$$

(S1)

where (x_0, y_0) is the center position, A is the background level, B is the peak intensity at (x_0, y_0), S_x and S_y are the standard deviations of the Gaussian distribution along the x- and y-axes, respectively. The localization precision depends on the photons collected from fluorescent

molecules and background noise level in each imaging period, as well as the pixel size of the camera. The localization precision (σ_j , $_{j=x, y}$) can be calculated according to equation S2(57):

$$\sigma_j = \sqrt{\left(\frac{S_j^2}{N} + \frac{a^2/12}{N} + \frac{8\pi S_j^4 b^2}{a^2 N^2}\right)}$$

(S2)

where N is the photons collected in each imaging frame, a is the pixel size, and b is the background noise in photons. In the specific example in Fig. S5, the localization precisions are determined to be $\sigma_x = 30$ nm, $\sigma_y = 21$ nm. The average localization precision is determined to be $\sigma_{xy} = 26$ nm using equation S3.

$$\sigma_{xy} = (\sigma_x + \sigma_y)/2 \tag{S3}$$
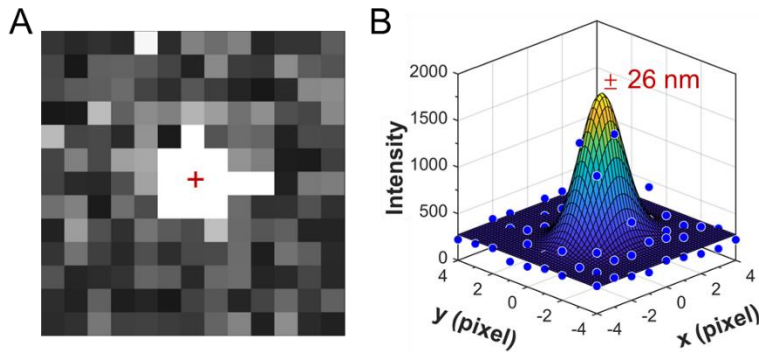
Fig. S5. Localize the center position of single molecules with nanometer precision. (A) Typical fluorescence image of a single fluorescein molecule on InSe during the photocatalytic reaction. (B) The center position of the fluorescein molecule is determined with nanometer precision ($\pm$ 26 nm) by 2D Gaussian fitting of the fluorescence intensity profile.

## Section S4. Identification of wrinkle and vacancy

Wrinkles can randomly form during the mechanical exfoliation and transfer of 2D layered materials. There are two types of wrinkles used in the single-molecule fluorescence imaging. One type of wrinkles is the edge of the folding layer, as shown in Fig. S6A-C. The other type of wrinkles is the wrinkling on the basal plane, as shown in Fig. S6D-F.
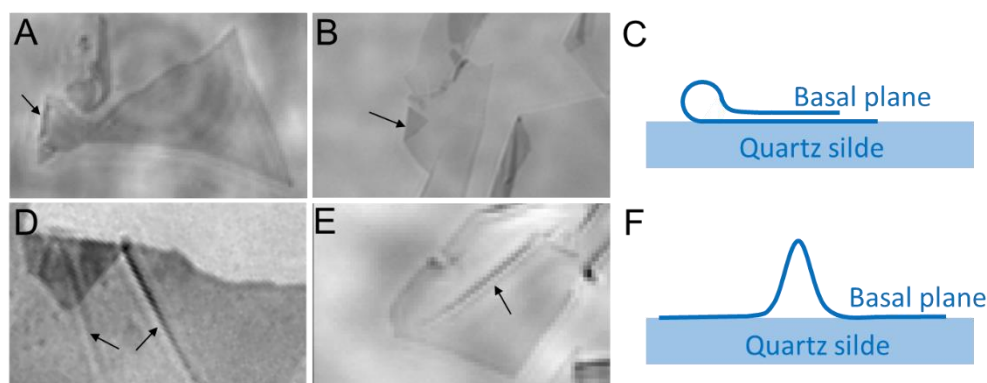

Fig. S6. Optical bright-field images and schematic diagrams of wrinkles on InSe flakes. Wrinkles are marked by arrows.

We attributed the small reactive sites to vacancy (e.g., single-atom vacancy or multiple-atoms vacancies) based on the consideration of two factors. First, no structural features were observed on the basal plane from the optical and AFM images, indicating that the reactive sites would be very small point defects. Second, it has been well studied that vacancies rather than other defects are formed on the basal plane during mechanical exfoliation[19, 20]. To further demonstrate the small reactive sites are vacancies in our experiments, we performed Argon (Ar) plasma treatment to create vacancies[21] on the basal plane of 2D layered InSe. InSe flakes were mechanical exfoliated and transferred on a quartz slide and treated with Ar plasma (7 W, 0.5 s). Fig. S7A and b show that the number of small reactive sites on the basal plane increased after the Ar plasma treatment. The reaction rate of the newly created reactive sites after Ar plasma treatment (Fig. S7D, 2.5 ± 0.1 s^{-1} μm^{-2}) is similar to that on the pristine 2D layered InSe (Fig. S7C, 2.8 ± 0.2 s^{-1} μm^{-2}). Furthermore, AFM images (Fig. S8) show that the topography of the basal plane remains the same before and after the Ar plasma treatment, indicating that only small vacancies were created.

We counted the hot spots in the localization mapping as vacancies based on two standards. First, the activity of the hot spot is higher than that on the nearby pristine InSe. Second, by comparing the activity mapping of InSe before and after Ar plasma, we can identify the position of vacancies and further determined the sizes of vacancies, as shown in Fig. S7F. Therefore, the size (FWHM) of the vacancies should be in the range of 110~290 nm.
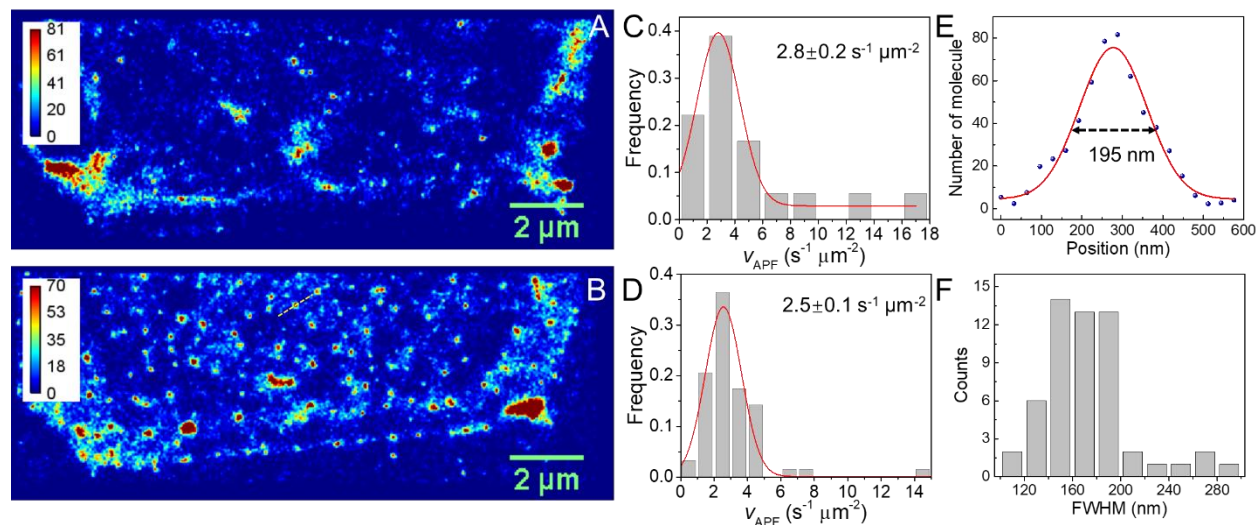
Fig. S7. Photocatalytic activity of the same 2D layered InSe before and after Ar plasma treatment. (A, B) Localization mapping of photocatalytic activities on a 6~8-layer InSe flake before (A) and after (B) Ar plasma treatment under 100 nM APF over the same imaging period. The color bar denotes the number of fluorescein molecules from chemical reaction that were detected. (C, D) Reaction rate of APF at the small reactive sites in (A) and (B). (E) Cross-profile plots of molecule numbers at vacancy marked in (B). (F) Statistic results of the sizes (FWHM) of 55 vacancies in (B).
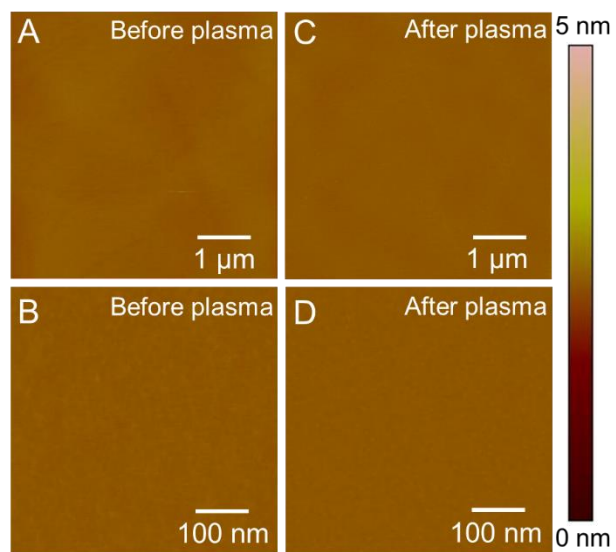
Fig. S8. AFM images of the basal plane of InSe before (A, B) and after (C, D) the same Ar plasma treatment used in Fig. S7.
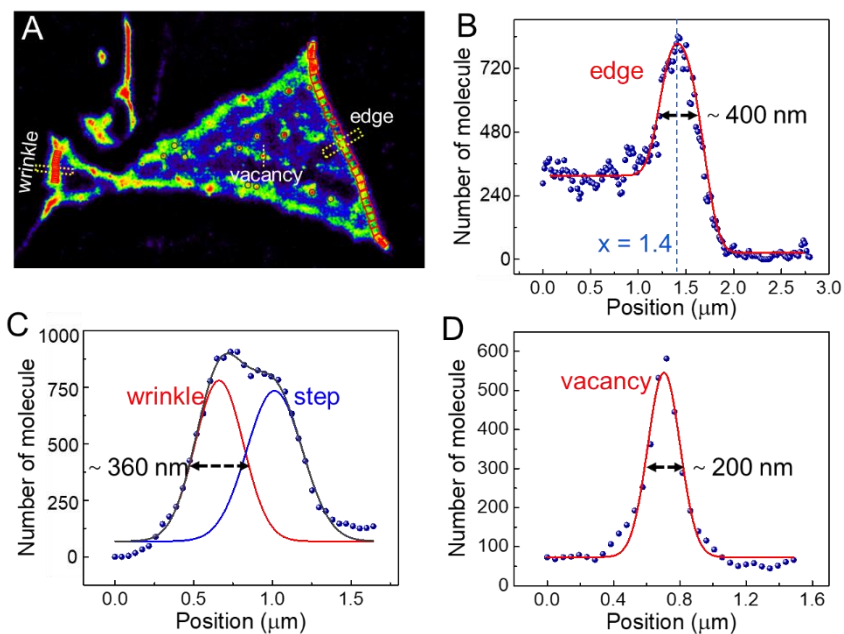
Section S5. Image segmentation

Image segmentation was applied before quantifying the catalytic activities and kinetics of each structural feature. Briefly, the size of the reaction region at each structural feature except basal plane was determined by the molecule number-position profile.

For the edge, we plot the molecule number as a function of position (Fig. S9B) which is cross-profile on the edge (marked in Fig. S9A). The number of molecules becomes larger at the edge, indicating a stronger photocatalytic ability. We fit the distribution using $I = \exp\left(-\frac{(x-a)^2}{b^2}\right) \otimes (step\ function)$, where step function = c, when x<1.4; and equal to d, when x≥1.4. We use the full width at half maximum (FWHM) ~ 400 nm from the fitting as the size of edge-related reaction region. Next, the edge is dissected into several regions with a size of 400 nm × 400 nm, as shown in Fig. S9A. In these small regions, we make sure that almost only one fluorescence burst exists in every frame (>99%). Otherwise, the size along the edge is decreased (e.g., 300 nm × 400 μm) to achieve this criterion.

Due to the mechanical exfoliation and transferring of InSe, it is possible for flakes to fold over onto themselves, forming a wrinkle with a folding angle of 180°. Fig. S9C is the plots of molecule number with the position across the wrinkle. It is the convolution of two reaction regions, with the more active one belongs to the wrinkle and the less active one belongs to the stepped edge. We can resolve the size of wrinkle-related reaction region (~360 nm) of the FWHM and dissect the wrinkle into several regions with a size of 50 nm × 360 nm (Fig. S9A). It should be noted that molecule densities in these small regions may be a little overestimated since they are slightly closed to the stepped edge. However, the photocatalytic activity of wrinkle is still in between that of edge and vacancy.

There exist some small reactive sites on the basal plane (Fig. S9A). However, no structural features can be observed from the optical (Fig. S6) and AFM (Fig. S8) images. These active sites are believed to be atomic scale vacancies, which usually can be observed during the mechanical exfoliation process(19, 20). As discussed in Section S4, the size (FWHM) of vacancies is in the range of 110~290 nm. In this specific example in Fig. S9A, the size of vacancy-related reaction region is in the range of 150~240 nm (Fig. S9D). The distinctly different sizes show the heterogeneity of vacancy structures, e.g., single-, double, and multi-atom vacancy. The size of

defect-related reaction region is much larger than actual size of defect. It may be a convolution of four factors. First, the spatial resolution of single-molecule imaging (tens of nanometers). Second, defect leads to the band bending and the varied carrier density results in a gradual change of electronic properties over the nearby pristine materials. The formed electronic property variation region between the defect and pristine martials has significant impacts on the catalytic activity(*4*) and the size of this region can be up to tens of nanometer(*8*). Third, a high concentration of hydroxyl radicals is generated at defects and could diffuse to the nearby pristine materials. Forth, the product molecule (fluorescein) diffuses on the InSe until it completely desorbs from the surface. For the basal plane, we dissected it into sub-regions with sizes of 400×400 nm for convenience. In our experiments, only one fluorescence burst exists in every frame using this segmentation method.

Fig. S9. Region analysis of localization mapping of single-molecule photocatalytic events on InSe flakes. (A) Image segmentation of different structural features. (B-D) Cross-profile plots of molecule numbers at the edge, wrinkle, and vacancy marked in (A), respectively.
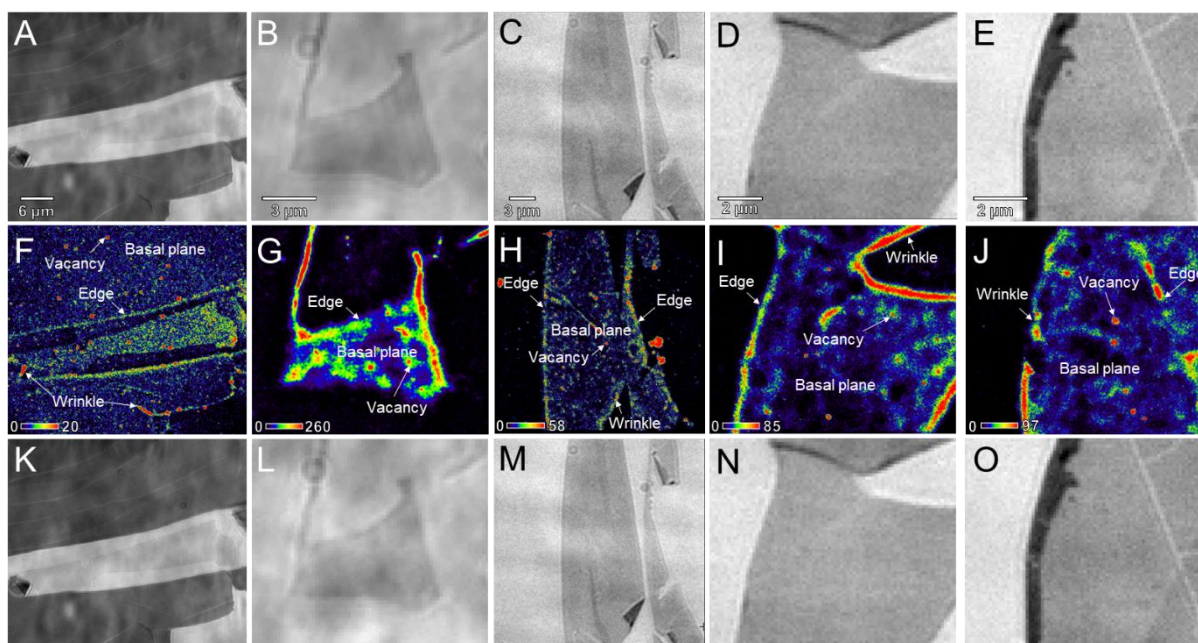
Fig. S10. Localization mapping of the photocatalytic activity on 7 InSe flakes. (A-E) Optical bright-field images of InSe flakes before photocatalytic reaction. (F-J) Localization mapping of the photocatalytic activity on InSe flakes. (K-O) Optical bright-field images of InSe flakes after photocatalytic reaction.
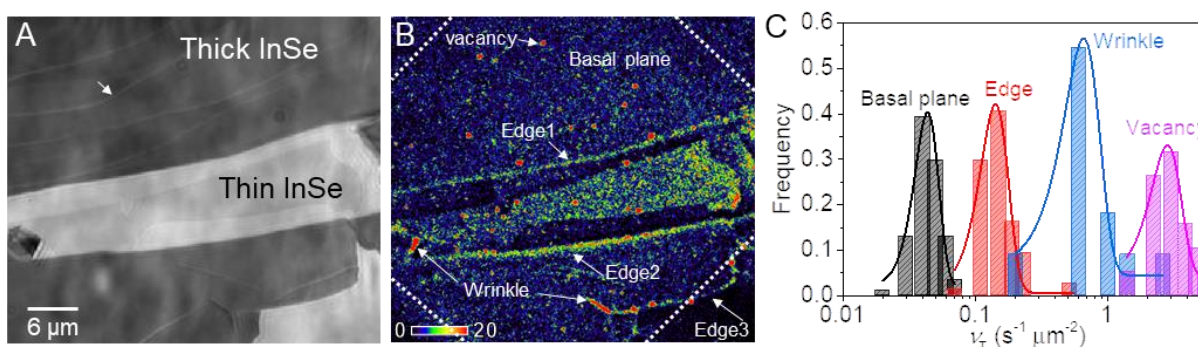
Fig. S11. Localization mapping of the photocatalytic activity on thick InSe. (A) Optical bright field image of InSe flakes. The grey line marked by the arrow is the crack under the InSe. (B) Localization mapping of photocatalytic activities on InSe flakes in (A) under 100 nM APF. Dash lines denote the contour of laser spot thus edge3 is excluded for further analysis. The color bar denotes the number of fluorescein molecules detected during the photocatalytic reaction over

50×50 nm^2 in the total collection period. (c) Turnover rate of different structural features in the thick InSe (black InSe in (a)) under 100 nM APF.

Fig. S11 is the localization mapping of single-molecule photocatalytic events on a thick InSe. After applying the image segmentation, we counted the single turn-over events and quantified the catalytic turnover rate at different structural features (i.e., basal plane, edge, wrinkle, and vacancy). As shown in Fig. S11C, we obtain the average turnover rate v_T of 0.044±0.009, 0.142±0.035, 0.659±0.209, and 2.830±0.747s^{-1} μm^{-2} at basal plane, edge, wrinkle, and vacancy, respectively at 100 nM APF in PBS buffer over a period of ~ 28 min. This result shows that vacancy has higher photocatalytic activity than edge and wrinkle.

Section S6. Quantification of photocatalytic kinetics on 2D layered InSe

Fig. 1C in the main text shows a segment of a typical fluorescence intensity trajectory from a region of 400 nm × 400 nm on the basal plane. The on-off of fluorescence intensity is associated to the catalytic reaction. τ_{off} is the waiting time before the individual catalytic event happens (Fig. S12A), reflecting the time period for product formation. τ_{on} is the waiting time for the product molecule dissociation after formation (Fig. S12B). From these two waiting times, we can calculate the APF reaction rate (v_{APF}) and fluorescein dissociation rate (v_d). Fitting the distribution of τ_{off} (Fig. S13A) and τ_{on} (Fig. S13B) using exponential decay function gives the characteristic average values, $<\tau_{off}>$ and $<\tau_{on}>$. The APF reaction rate v_{APF} is determined as $<\tau_{off}>^{-1}$/Area and the fluorescein dissociation rate v_d is determined as $<\tau_{on}>^{-1}$. Fig. S13C, D show the distributions of v_{APF} and v_d over 34 reactive-regions along the edge and the data points were fitted with a simple Gaussian function giving an average reaction rate of $v_{APF} = 2.263 \pm 0.120$ s^{-1} μm^{-2} and a dissociation rate of $v_d = 5.312 \pm 0.218$ s^{-1}. This process was repeated for measuring the reaction and dissociation rates of different structural features under variable APF concentrations.
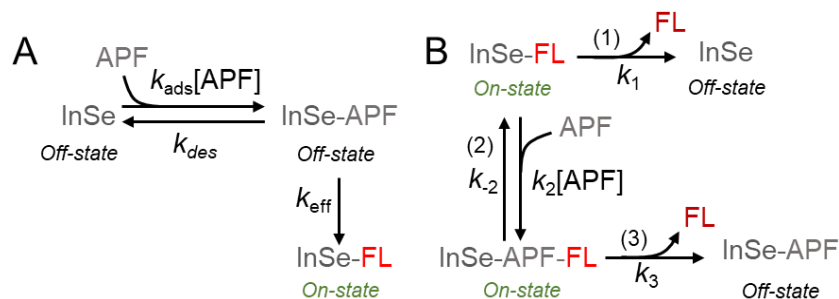
Fig. S12. Schematic diagrams of the reaction and dissociation mechanisms during τ_{off} (A) and τ_{on} (B), respectively. FL denotes the product molecule, fluorescein. k_{ads} and k_{des} are the adsorption and desorption rate constants of APF, respectively.
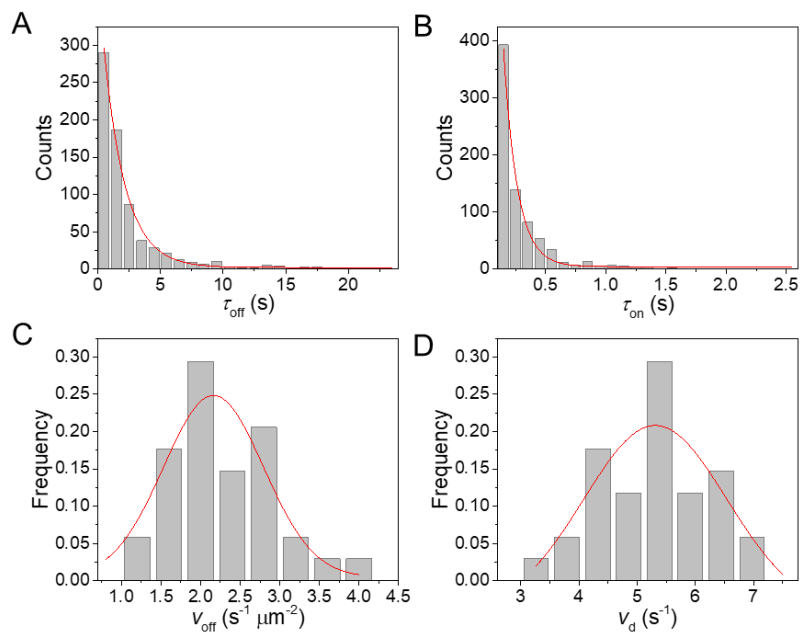
Fig. S13. Quantification of catalytic reaction rate and product dissociation rate. (A, B) Fitting the distribution of τ_{off} (A) and τ_{on} (B) using exponential decay function gives the characteristic average values, $<\tau_{off}> = 3.144 \pm 0.171$ s and $<\tau_{on}> = 0.151 \pm 0.006$ s. (C, D) Gaussian fitting the distribution of catalytic reaction rates (C) and product dissociation rates (D) over 34 reactive-regions along the edge at 0.1 µM of APF with a flow rate of 20 µL min^{-1} gives a reaction rate of $v_{APF} = 2.263 \pm 0.120$ s^{-1} µm^{-2} and a dissociation rate of $v_d = 5.312 \pm 0.218$ s^{-1}.

Section S7. Electronic band alignments between basal plane and defects

Regarding the wrinkle used in the single-molecule fluorescence imaging, both the tensile and compressive strain exist(*30*), as shown in Fig. S14A. For the wrinkle, as shown in Fig. S14B, with the increasing tensile strain the bandgap decreases monotonically with the conduction band bending downward and valance band bending upward(*31-34*), forming a type-I band alignment with the pristine InSe (Fig. S14C). In this type of band alignment, both photogenerated electrons and holes accumulate at the wrinkle due to the funnel effect(*58*). Although most of the electrons and holes at the wrinkle still undergo the recombination, this accumulation increases the total amount of photogenerated electrons and holes at the wrinkle, thus inducing a higher photocatalytic activity than the basal plane. In contrast, with the increasing compressive strain, both the conduction band and valence band bend upward(*31-34*), forming a type-II band alignment with the pristine InSe (Fig. S14D). The built-in field in this alignment accelerates the electron-hole separation, prevents the recombination, and further increases the photocatalytic activity.

For the unsaturated edge and vacancy, they can be easily oxidized and form In-O bonds(*35-37, 59*). The different valent states of indium ions create the type-II band alignment between the oxidized defects and the nearby pristine InSe(*34, 38*), as illustrated in Fig. S14E. The built-in field in this alignment further accelerates the electron-hole separation and prevents the recombination. Thus, the edges and vacancies natively have higher photocatalytic activity.
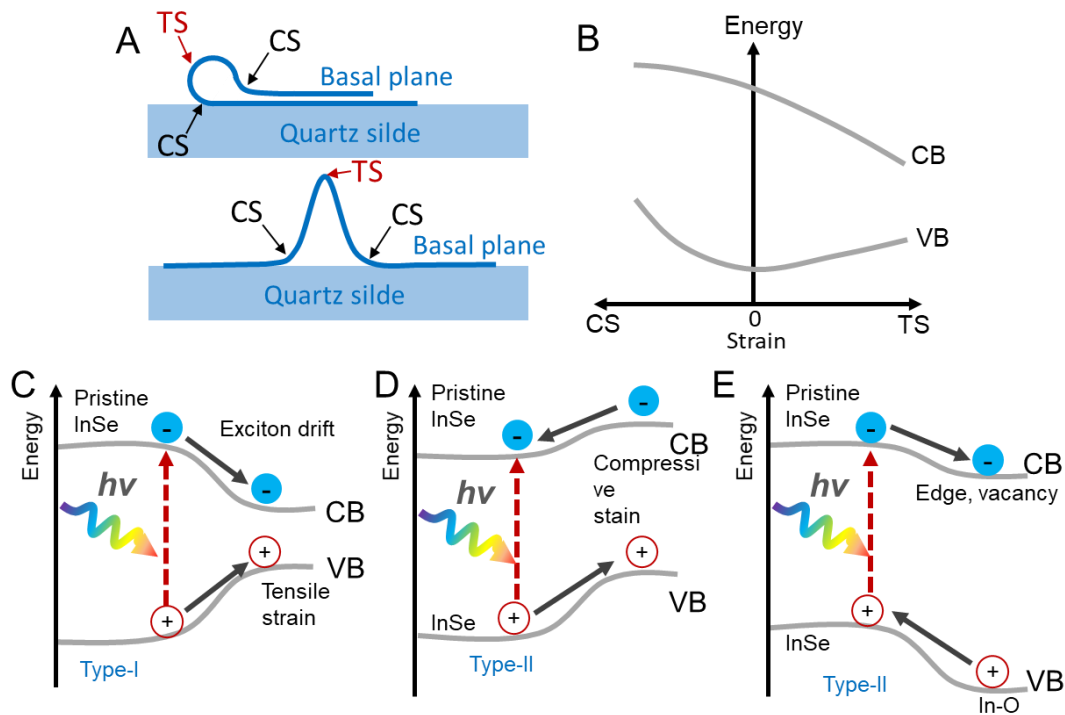
Fig. S14. Schematic diagrams of electronic band alignments between pristine InSe and defects. (A) Strain distribution along the wrinkles. TS and CS denote tensile strain and compressive strain, respectively. (B) Schematic of the strain dependence of the relative band edge positions of InSe. CB and VB denote as conduction band and valance band, respectively. (C-E) Schematic of relative band edge positions between pristine InSe and tensile wrinkle (C), pristine InSe and compressive wrinkle (D), pristine InSe and edge/vacancy (E).

Section S8. Identification of InSe layer number

Since it is difficult to do the atomic force microscopy (AFM) measurements of InSe samples in the flow cell after the single-molecule experiments, we employed optical contrast of the InSe and quartz by the reflection optical microscopy ($C = (I_{quartz} - I_{InSe})/I_{quartz}$). By combing the measurement of AFM and optical contrast, we establish the working curve of layer-dependent optical contrast of InSe flakes on quartz slide. With the increase of layer number, the optical contrast decreases.
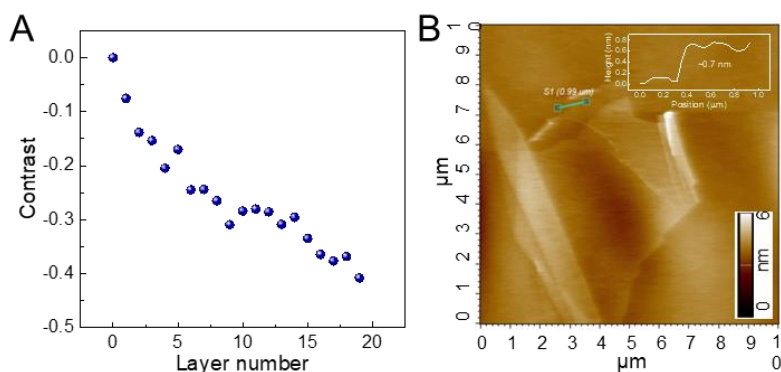
Fig. S15. Identification of InSe layer number. (A) Layer-dependent optical contrast of InSe on quartz slide. (B) AFM image of InSe flakes on quartz. Inset is the height curve of a monolayer marked by green line in the AFM image.

Section S9. The influence of variable surface properties of 2D layered InSe on the catalytic kinetics

It has been found that the catalytic sites, where the catalytic reaction occurs, are different from the docking sites, where the dissociation occurs(*25*). Similar phenomenon also can be observed in 2D layered InSe catalyst. Fig. S16A shows a single-turnover trajectory at an active site (vacancy) at 1 μM APF. The variable time-dependent turnover rate indicates the dynamic photocatalytic activity fluctuation of the active site. This activity fluctuation could be due to the change of the surface electronic property induced by the electron and hole excitation and separation by light illumination, and the surface reconstruction originates from the distortion of the original lattice structure symmetry(*60*). Variations of active site properties would modulate the APF reaction and the dissociation rates, which dominate τ_{off} and τ_{on} under high APF concentration, respectively. However, the difference in the fluctuation rate of τ_{off} and τ_{on} (Fig. S16B) indicates that they experience distinct surface property changing dynamics. Therefore, the catalytic sites are different from the docking sites and the product (fluorescein) would diffuse on the surface until it completely desorbs from the InSe surface.
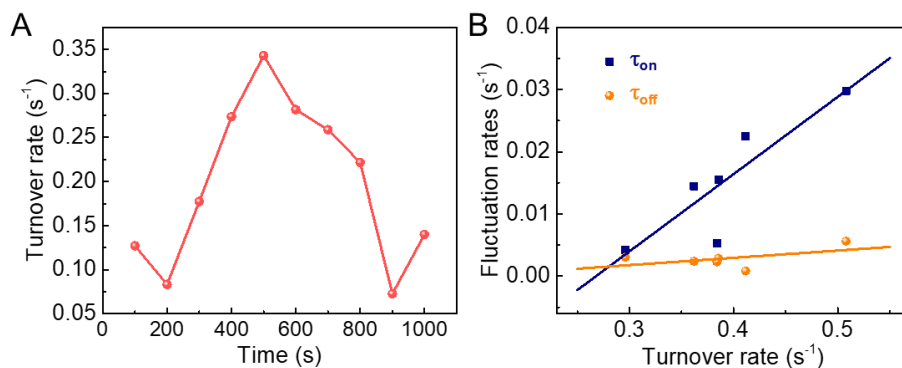

Fig. S16. Photocatalytic activity dynamics. (A) Trajectory of fluctuating turnover rate in a vacancy at 1 μM APF. Data points are calculated every 100 s. (B) Dependence of the activity fluctuation rate (the inverse of fluctuation correlation time) on the turnover rates.

Section S10. Surface diffusion of fluorescein on 2D layered InSe

To define the diffusion behavior on 2D layered InSe, we first calculated the localization uncertainty of fluorescein at different structural features, as shown in Fig. S17A-D. If displacements of more than 75% steps in a track is below twice the localization uncertainty (110, 81, 80, 76 nm for the basal plane, edge, wrinkle, and vacancy, respectively), we defined it as the immobile behavior. If this fraction is below 25%, we defined it as the mobile diffusion. The residual tracks, which consist of immobile and mobile behaviors, were defined as hybrid diffusion. We classified 453, 477, 453, 938 tracks at the basal plane, edge, wrinkle, and vacancy, respectively. The fractions of three diffusion behaviors at different structural features was shown in Table S1.

Fig. S18 illustrates the conventional view of energy diagram of surface desorption and diffusion(*52*). The activation energy of diffusion is smaller than that of the direct desorption, indicating that the desorption during the diffusion is easier than the direct desorption from the adsorption sites on the surface(*49-52*). Hence, direct desorption is slower than the desorption through the desorption-mediated diffusion.
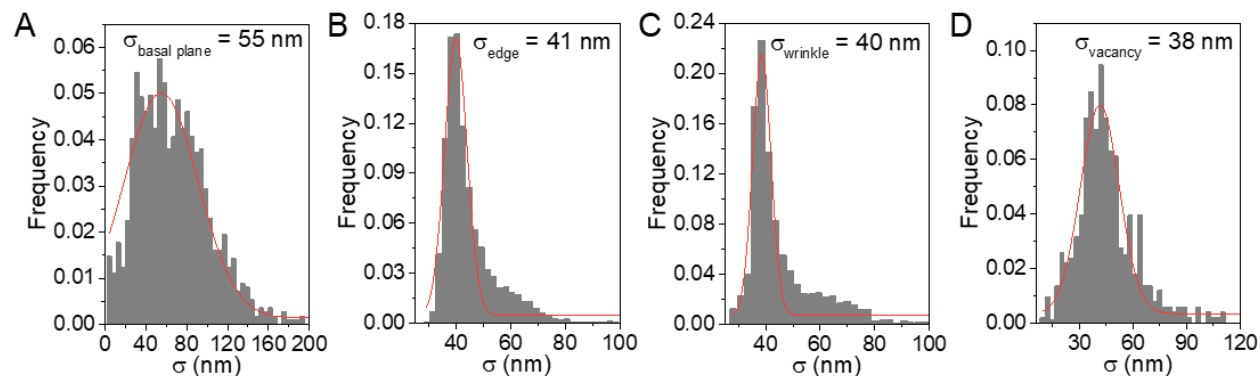
Fig. S17. Single-molecule fluorescence imaging reveals the diffusion behaviors of fluorescein on InSe surface. (A-D) Localization uncertainty in determining molecular positions at different structural features: basal plane (A), edge (B), wrinkle (C), and vacancy (D).

Table S1. The fractions of three diffusion behaviors at different structural features.

	Immobile	Hybrid	Mobile
Basal plane	22%	49%	29%
Edge	10%	60%	30%
Wrinkle	16%	72%	12%
Vacancy	31%	64%	5%
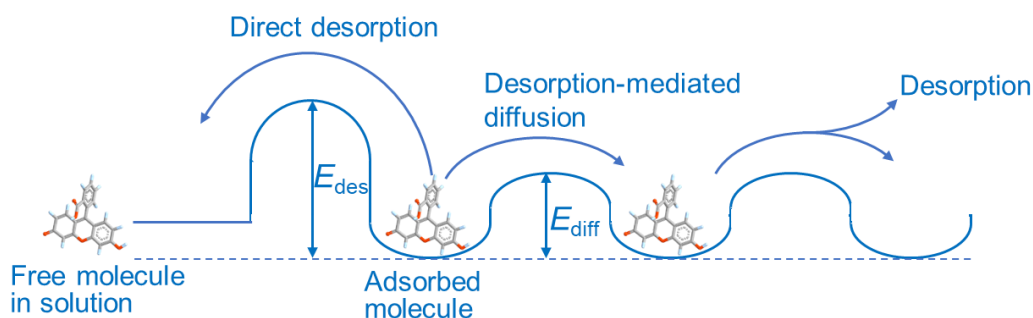
Fig. S18. Schematic energy diagram of surface desorption and diffusion.

The diffusion of fluorescein on InSe surface follows the random-walk mechanism. The probability that a molecule from the origin will be found at time t within a displacement r is fitted with the probability density function(*15*):

$$p(r^2, t) \cdot dr^2 = \frac{1}{\pi \langle r_{(t)}^2 \rangle} \exp\left(\frac{-r_{(t)}^2}{\langle r_{(t)}^2 \rangle + \sigma^2}\right) 2\pi r \cdot dr^2 \quad \dots\dots\dots\dots\dots\dots\dots\dots\dots\dots\dots\dots(1)$$

where $\langle r^2 \rangle$ is the mean square displacement and σ is the localization uncertainty. The diffusion coefficient was determined according to the Einstein-Smoluchowski equation for random diffusion in two dimensions(*13*).

$$\langle r_{(t)}^2 \rangle = 4Dt \quad \dots\dots\dots\dots\dots\dots\dots\dots\dots\dots\dots\dots\dots\dots\dots\dots\dots\dots\dots..\dots\dots\dots\dots\dots..(2)$$

Fig. S19A shows a typical distribution of the displacement of fluorescein diffusion in a sub-region at the edge. Fitting the distribution with the equation 1 gives the mean squared displacement

$\langle r^2 \rangle$ and subsequently the D_{eff} is determined by equation 2. Fig. S19B shows the distribution of D_{eff} over 80 sub-regions along the edge and the data points were fitted with a simple Gaussian function giving an average reaction rate of $D_{eff} = 0.058\pm0.004$ μm^2 s^{-1}. This process was repeated for measuring the diffusion coefficients of different structural features.
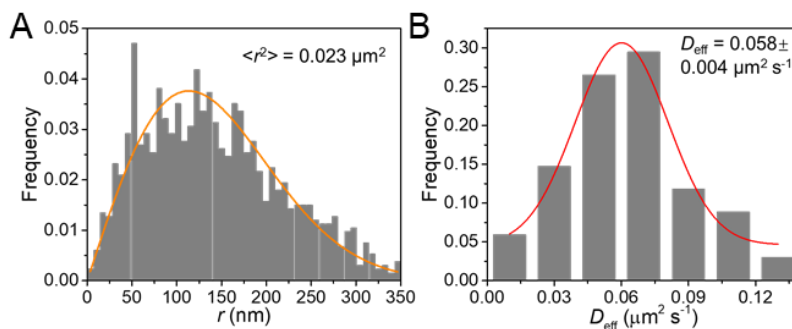
Fig. S19. Diffusion coefficients of fluorescein on InSe surface. (A) The distribution of the displacement during the diffusion of fluorescein. The data was fitted using radial probability density function to determine the mean squared displacement $\langle r^2 \rangle$. (B) Gaussian fitting the distribution of the diffusion coefficients from more than 80 sub-regions at the edge.

REFERENCES AND NOTES

1. H. Zhang, R. Lv, Defect engineering of two-dimensional materials for efficient electrocatalysis. *J. Materiomics* **4**, 95–107 (2018).

2. X. Chia, M. Pumera, Characteristics and performance of two-dimensional materials for electrocatalysis. *Nat. Catal.* **1**, 909–921 (2018).

3. T. F. Jaramillo, K. P. Jorgensen, J. Bonde, J. H. Nielsen, S. Horch, I. Chorkendorff, Identification of active edge sites for electrochemical H_2 evolution from MoS_2 nanocatalysts. *Science* **317**, 100–102 (2007).

4. Z. Lin, B. R. Carvalho, E. Kahn, R. Lv, R. Rao, H. Terrones, M. A. Pimenta, M. Terrones, Defect engineering of two-dimensional transition metal dichalcogenides. *2D Mater.* **3**, 022002 (2016).

5. Z. Wu, Z. Ni, Spectroscopic investigation of defects in two-dimensional materials. *Nanophotonics* **6**, 1219–1237 (2017).

6. W. Zhou, X. Zou, S. Najmaei, Z. Liu, Y. Shi, J. Kong, J. Lou, P. M. Ajayan, B. I. Yakobson, J.-C. Idrobo, Intrinsic structural defects in monolayer molybdenum disulfide. *Nano Lett.* **13**, 2615–2622 (2013).

7. Y. L. Huang, Y. Chen, W. Zhang, S. Y. Quek, C.-H. Chen, L.-J. Li, W.-T. Hsu, W.-H. Chang, Y. J. Zheng, W. Chen, A. T. S. Wee, Bandgap tunability at single-layer molybdenum disulphide grain boundaries. *Nat. Commun.* **6**, 6298 (2015).

8. T.-X. Huang, X. Cong, S.-S. Wu, K.-Q. Lin, X. Yao, Y.-H. He, J.-B. Wu, Y.-F. Bao, S.-C. Huang, X. Wang, P.-H. Tan, B. Ren, Probing the edge-related properties of atomically thin MoS_2 at nanoscale. *Nat. Commun.* **10**, 5544 (2019).

9. Y. Luo, R. Engelke, M. Mattheakis, M. Tamagnone, S. Carr, K. Watanabe, T. Taniguchi, E. Kaxiras, P. Kim, W. L. Wilson, In situ nanoscale imaging of moiré superlattices in twisted van der Waals heterostructures. *Nat. Commun.* **11**, 4209 (2020).

10. D. Deng, K. S. Novoselov, Q. Fu, N. Zheng, Z. Tian, X. Bao, Catalysis with two-dimensional materials and their heterostructures. *Nat. Nanotechnol.* **11**, 218–230 (2016).

11. X. Zhou, N. M. Andoy, G. Liu, E. Choudhary, K.-S. Han, H. Shen, P. Chen, Quantitative super-resolution imaging uncovers reactivity patterns on single nanocatalysts. *Nat. Nanotechnol.* **7**, 237–241 (2012).

12. K. Naito, T. Tachikawa, M. Fujitsuka, T. Majima, Single-molecule observation of photocatalytic reaction in TiO_2 nanotube: Importance of molecular transport through porous structures. *J. Am. Chem. Soc.* **131**, 934–936 (2009).

13. M. B. J. Roeffaers, B. F. Sels, H. Uji-i, F. C. De Schryver, P. A. Jacobs, D. E. De Vos, J. Hofkens, Spatially resolved observation of crystal-face-dependent catalysis by single turnover counting. *Nature* **439**, 572–575 (2006).

14. B. Dong, Y. Pei, N. Mansour, X. Lu, K. Yang, W. Huang, N. Fang, Deciphering nanoconfinement effects on molecular orientation and reaction intermediate by single molecule imaging. *Nat. Commun.* **10**, 4815 (2019).

15. B. Dong, Y. Pei, F. Zhao, T. W. Goh, Z. Qi, C. Xiao, K. Chen, W. Huang, N. Fang, In situ quantitative single-molecule study of dynamic catalytic processes in nanoconfinement. *Nat. Catal.* **1**, 135–140 (2018).

16. B. Dong, N. Mansour, Y. Pei, Z. Wang, T. Huang, S. L. Filbrun, M. Chen, X. Cheng, M. Pruski, W. Huang, N. Fang, Single molecule investigation of nanoconfinement hydrophobicity in heterogeneous catalysis. *J. Am. Chem. Soc.* **142**, 13305–13309 (2020).

17. T. Tachikawa, S. Yamashita, T. Majima, Probing photocatalytic active sites on a single titanosilicate zeolite with a redox-responsive fluorescent dye. *Angew. Chem. Int. Ed.* **49**, 432–435 (2010).

18. T. Tachikawa, P. Zhang, Z. Bian, T. Majima, Efficient charge separation and photooxidation on cobalt phosphate-loaded TiO_2 mesocrystal superstructures. *J. Mater. Chem. A* **2**, 3381–3388 (2014).

19. P. Vancsó, G. Z. Magda, J. Pető, J.-Y. Noh, Y.-S. Kim, C. Hwang, L. P. Biró, L. Tapasztó, The intrinsic defect structure of exfoliated MoS_2 single layers revealed by scanning tunneling microscopy. *Sci. Rep.* **6**, 29726 (2016).

20. J. Pető, T. Ollár, P. Vancsó, Z. I. Popov, G. Z. Magda, G. Dobrik, C. Hwang, P. B. Sorokin, L. Tapasztó, Spontaneous doping of the basal plane of MoS_2 single layers through oxygen substitution under ambient conditions. *Nat. Chem.* **10**, 1246–1251 (2018).

21. H. Li, C. Tsai, A. L. Koh, L. Cai, A. W. Contryman, A. H. Fragapane, J. Zhao, H. S. Han, H. C. Manoharan, F. Abild-Pedersen, J. K. Norskov, X. Zheng, Activating and optimizing MoS_2 basal planes for hydrogen evolution through the formation of strained sulphur vacancies. *Nat. Mater.* **15**, 48–53 (2016).

22. D. Axelrod, Total internal reflection fluorescence microscopy, in *Methods in Cell Biology* (2008), vol. 89, pp. 169–221.

23. L. Song, R. P. M. van Gijlswijk, I. T. Young, H. J. Tanke, Influence of fluorochrome labeling density on the photobleaching kinetics of fluorescein in microscopy. *Cytometry* **27**, 213–223 (1997).

24. L. Song, E. Hennink, I. T. Young, H. J. Tanke, Photobleaching kinetics of fluorescein in quantitative fluorescence microscopy. *Biophys. J.* **68**, 2588–2600 (1995).

25. W. Xu, J. S. Kong, Y.-T. E. Yeh, P. Chen, Single-molecule nanocatalysis reveals heterogeneous reaction pathways and catalytic dynamics. *Nat. Mater.* **7**, 992–996 (2008).

26. W. Xu, J. S. Kong, P. Chen, Single-molecule kinetic theory of heterogeneous and enzyme catalysis. *J. Phys. Chem. C* **113**, 2393–2404 (2009).

27. W. Xu, H. Shen, G. Liu, P. Chen, Single-molecule kinetics of nanoparticle catalysis. *Nano Res.* **2**, 911–922 (2009).

28. H. Shen, W. Xu, P. Chen, Single-molecule nanoscale electrocatalysis. *Phys. Chem. Chem. Phys.* **12**, 6555–6563 (2010).

29. K. S. Han, G. Liu, X. Zhou, R. E. Medina, P. Chen, How does a single Pt nanocatalyst behave in two different reactions? A single-molecule study *Nano Lett.* **12**, 1253–1259 (2012).

30. D. J. Trainer, Y. Zhang, F. Bobba, X. Xi, S.-W. Hla, M. Iavarone, The effects of atomic-scale strain relaxation on the electronic properties of monolayer MoS_2. *ACS Nano* **13**, 8284–8291 (2019).

31. H. Yang, P. Zhao, Y. Ma, X. Lv, B. Huang, Y. Dai, Janus single-layer group-III monochalcogenides: A promising visible-light photocatalyst. *J. Phys. D Appl. Phys.* **52**, 455303 (2019).

32. B. Wang, H. Yuan, J. Chang, X. Chen, H. Chen, Two dimensional $InSe/C_2N$ van der Waals heterojunction as enhanced visible-light-responsible photocatalyst for water splitting. *Appl. Surf. Sci.* **485**, 375–380 (2019).

33. M. Wu, J.-j. Shi, M. Zhang, Y.-m. Ding, H. Wang, Y.-l. Cen, J. Lu, Enhancement of photoluminescence and hole mobility in 1- to 5-layer InSe due to the top valence-band inversion: Strain effect. *Nanoscale* **10**, 11441–11451 (2018).

34. Y. Liang, C. Long, J. Li, H. Jin, B. Huang, Y. Dai, InSe monolayer: Promising cocatalyst of $g-C_3N_4$ for water splitting under visible light. *ACS Appl. Energy Mater.* **1**, 5394–5401 (2018).

35. K. J. Xiao, A. Carvalho, A. H. Castro Neto, Defects and oxidation resilience in InSe. *Phys. Rev. B* **96**, 054112 (2017).

36. C.-H. Ho, C.-H. Lin, Y.-P. Wang, Y.-C. Chen, S.-H. Chen, Y.-S. Huang, Surface oxide effect on optical sensing and photoelectric conversion of $\alpha-In_2Se_3$ hexagonal microplates. *ACS Appl. Mater. Interfaces* **5**, 2269–2277 (2013).

37. A. A. Kistanov, Y. Cai, K. Zhou, S. V. Dmitriev, Y.-W. Zhang, Atomic-scale mechanisms of defect- and light-induced oxidation and degradation of InSe. *J. Mater. Chem. C* **6**, 518–525 (2018).

38. X. Wei, C. Dong, A. Xu, X. Li, D. D. Macdonald, Oxygen-induced degradation of the electronic properties of thin-layer InSe. *Phys. Chem. Chem. Phys.* **20**, 2238–2250 (2018).

39. J. Zhang, P. Zhou, J. Liu, J. Yu, New understanding of the difference of photocatalytic activity among anatase, rutile and brookite TiO$_2$. *Phys. Chem. Chem. Phys.* **16**, 20382–20386 (2014).

40. O. H. Pakarinen, J. M. Mativetsky, A. Gulans, M. J. Puska, A. S. Foster, P. Grutter, Role of van der Waals forces in the adsorption and diffusion of organic molecules on an insulating surface. *Phys. Rev. B* **80**, 085401 (2009).

41. M. Pandey, K. S. Thygesen, Two-dimensional MXenes as catalysts for electrochemical hydrogen evolution: A computational screening study. *J. Phys. Chem. C* **121**, 13593–13598 (2017).

42. J. Shang, L. Pan, X. Wang, J. Li, Z. Wei, Tunable electric properties of bilayer InSe with different interlayer distances and external electric field. *Semicond. Sci. Tech.* **33**, 034002 (2018).

43. M. J. Hamer, J. Zultak, A. V. Tyurnina, V. Zólyomi, D. Terry, A. Barinov, A. Garner, J. Donoghue, A. P. Rooney, V. Kandyba, A. Giampietri, A. Graham, N. Teutsch, X. Xia, M. Koperski, S. J. Haigh, V. I. Fal'ko, R. V. Gorbachev, N. R. Wilson, Indirect to direct gap crossover in two-dimensional InSe revealed by angle-resolved photoemission spectroscopy. *ACS Nano* **13**, 2136–2142 (2019).

44. G. W. Mudd, M. R. Molas, X. Chen, V. Zólyomi, K. Nogajewski, Z. R. Kudrynskyi, Z. D. Kovalyuk, G. Yusa, O. Makarovsky, L. Eaves, M. Potemski, V. I. Fal'ko, A. Patanè, The direct-to-indirect band gap crossover in two-dimensional van der Waals Indium Selenide crystals. *Sci. Rep.* **6**, 39619 (2016).

45. M. Brotons-Gisbert, D. Andres-Penares, J. Suh, F. Hidalgo, R. Abargues, P. J. Rodríguez-Cantó, A. Segura, A. Cros, G. Tobias, E. Canadell, P. Ordejón, J. Wu, J. P. Martínez-Pastor, J. F. Sánchez-Royo, Nanotexturing to enhance photoluminescent response of atomically thin Indium Selenide with highly tunable band Gap. *Nano Lett.* **16**, 3221–3229 (2016).

46. T. Tian, C.-J. Shih, Molecular epitaxy on two-dimensional materials: The interplay between interactions. *Ind. Eng. Chem. Res.* **56**, 10552–10581 (2017).

47. W. Xu, J. S. Kong, P. Chen, Probing the catalytic activity and heterogeneity of Au-nanoparticles at the single-molecule level. *Phys. Chem. Chem. Phys.* **11**, 2767–2778 (2009).

48. M. J. Skaug, J. N. Mabry, D. K. Schwartz, Single-molecule tracking of polymer surface diffusion. *J. Am. Chem. Soc.* **136**, 1327–1332 (2014).

49. M. J. Skaug, A. M. Lacasta, L. Ramirez-Piscina, J. M. Sancho, K. Lindenberg, D. K. Schwartz, Single-molecule diffusion in a periodic potential at a solid–liquid interface. *Soft Matter* **10**, 753–759 (2014).

50. M. J. Skaug, J. Mabry, D. K. Schwartz, Intermittent molecular hopping at the solid-liquid interface. *Phys. Rev. Lett.* **110**, 256101 (2013).

51. R. Walder, N. Nelson, D. K. Schwartz, Single molecule observations of desorption-mediated diffusion at the solid-liquid interface. *Phys. Rev. Lett.* **107**, 156102 (2011).

52. B. B. Langdon, M. Kastantin, D. K. Schwartz, Apparent activation energies associated with protein dynamics on hydrophobic and hydrophilic surfaces. *Biophys. J.* **102**, 2625–2633 (2012).

53. S. Lei, L. Ge, S. Najmaei, A. George, R. Kappera, J. Lou, M. Chhowalla, H. Yamaguchi, G. Gupta, R. Vajtai, A. D. Mohite, P. M. Ajayan, Evolution of the electronic band structure and efficient photo-detection in atomic layers of InSe. *ACS Nano* **8**, 1263–1272 (2014).

54. K. S. Novoselov, A. K. Geim, S. V. Morozov, D. Jiang, M. I. Katsnelson, I. V. Grigorieva, S. V. Dubonos, A. A. Firsov, Two-dimensional gas of massless Dirac fermions in graphene. *Nature* **438**, 197–200 (2005).

55. A. Castellanos-Gomez, M. Buscema, R. Molenaar, V. Singh, L. Janssen, D. Z. Van, S. J. Herre, G. A. Steele, Deterministic transfer of two-dimensional materials by all-dry viscoelastic stamping. *2D Mater.* **1**, 011002 (2013).

56. K.-i. Setsukinai, Y. Urano, K. Kakinuma, H. J. Majima, T. Nagano, Development of novel fluorescence probes that can reliably detect reactive oxygen species and distinguish specific species. *J. Biol. Chem.* **278**, 3170–3175 (2003).

57. R. E. Thompson, D. R. Larson, W. W. Webb, Precise nanometer localization analysis for individual fluorescent probes. *Biophys. J.* **82**, 2775–2783 (2002).

58. A. Castellanos-Gomez, R. Roldán, E. Cappelluti, M. Buscema, F. Guinea, H. S. J. van der Zant, G. A. Steele, Local strain engineering in atomically thin MoS$_2$. *Nano Lett.* **13**, 5361–5366 (2013).

59. A. Politano, G. Chiarello, R. Samnakay, G. Liu, B. Gürbulak, S. Duman, A. A. Balandin, D. W. Boukhvalov, The influence of chemical reactivity of surface defects on ambient-stable InSe-based nanodevices. *Nanoscale* **8**, 8474–8479 (2016).

60. P. Lazar, M. Otyepka, Role of the edge properties in the hydrogen evolution reaction on MoS$_2$. *Chem. A Eur. J.* **23**, 4863–4869 (2017).